

CORONAL MAGNETIC FIELD MEASUREMENT FROM EUV IMAGES MADE BY THE SOLAR DYNAMICS OBSERVATORY

NAT GOPALSWAMY¹, NARIAKI NITTA², SACHIKO AKIYAMA^{1,3}, PERTTI MÄKELÄ^{1,3}, AND SEIJI YASHIRO^{1,3}

¹ NASA Goddard Space Flight Center, Greenbelt, MD 20771-0001 USA

² Lockheed-Martin Solar and Astrophysics Laboratory, Palo Alto, CA 94304, USA

³ The Catholic University of America, Washington, DC 20064, USA

Received 2011 May 29; accepted 2011 September 13; published 2011 December 14

ABSTRACT

By measuring the geometrical properties of the coronal mass ejection (CME) flux rope and the leading shock observed on 2010 June 13 by the *Solar Dynamics Observatory* (*SDO*) mission's Atmospheric Imaging Assembly we determine the Alfvén speed and the magnetic field strength in the inner corona at a heliocentric distance of ~ 1.4 Rs. The basic measurements are the shock standoff distance (ΔR) ahead of the CME flux rope, the radius of curvature of the flux rope (R_c), and the shock speed. We first derive the Alfvénic Mach number (M) using the relationship, $\Delta R/R_c = 0.81[(\gamma - 1)M^2 + 2]/[(\gamma + 1)(M^2 - 1)]$, where γ is the only parameter that needed to be assumed. For $\gamma = 4/3$, the Mach number declined from 3.7 to 1.5 indicating shock weakening within the field of view of the imager. The shock formation coincided with the appearance of a type II radio burst at a frequency of ~ 300 MHz (harmonic component), providing an independent confirmation of the shock. The shock compression ratio derived from the radio dynamic spectrum was found to be consistent with that derived from the theory of fast-mode MHD shocks. From the measured shock speed and the derived Mach number, we found the Alfvén speed to increase from ~ 140 km s $^{-1}$ to 460 km s $^{-1}$ over the distance range 1.2–1.5 Rs. By deriving the upstream plasma density from the emission frequency of the associated type II radio burst, we determined the coronal magnetic field to be in the range 1.3–1.5 G. The derived magnetic field values are consistent with other estimates in a similar distance range. This work demonstrates that the EUV imagers, in the presence of radio dynamic spectra, can be used as coronal magnetometers.

Key words: magnetic fields – shock waves – Sun: corona – Sun: coronal mass ejections (CMEs) – Sun: radio radiation

Online-only material: animation, color figures

1. INTRODUCTION

The idea of a shock standing ahead of a magnetic structure ejected from the Sun was proposed by Gold (1955, 1962), which was soon confirmed by space observations (Sonett et al. 1964). Extensive theory of the shock standoff distance has been developed for Earth's bow shock (see, e.g., Bennett et al. 1997 and references therein). Russell & Mulligan (2002) applied the standoff distance derived by Farris & Russell (1994) to the case of a shock driven by an interplanetary flux rope (magnetic cloud) to explain the curvature of the flux rope derived from in situ observations. Gopalswamy & Yashiro (2011) demonstrated that the method can be applied to shocks driven by flux rope coronal mass ejections (CMEs) observed in the *Solar and Heliospheric Observatory*/Large Angle and Spectrometric Coronagraph Experiment (*SOHO/LASCO*) images at several solar radii from the Sun. White-light shock structures are observed for relatively fast CMEs (Gopalswamy et al. 2009; Ontiveros & Vourlidas 2009). In this paper, we apply the standoff distance technique to a CME-driven shock observed on 2010 June 13 in the EUV images obtained by the Atmospheric Imaging Assembly (AIA; Lemen et al. 2011) on board the *Solar Dynamics Observatory* (*SDO*; Schwer et al. 2002). Gopalswamy & Yashiro (2011) had computed the ambient density in the corona using the polarized brightness image of the corona, but here we derived the density from the accompanying type II radio burst observed by the Hiraishi Radio Spectrograph (HiRAS) in Japan (Kondo et al. 1997).

2. OBSERVATIONS AND ANALYSIS

The 2010 June 13 CME was observed in several EUV wavelengths by *SDO/AIA*. Here, we use the AIA 193 Å images. The CME was described as a bubble by Patsourakos et al. (2010), who treated the CME as a sphere and reported on the early kinematics of the CME. Here we focus on the overlying shock structure that surrounds the flux rope and its standoff distance. Physical properties of the shock structure have also been reported by Ma et al. (2011). Kozarev et al. (2011) also identified the shock wave and reported on the implications for a possible solar energetic particle event. Unlike these authors, we focus on the standoff distance of the shock as a function of the heliocentric distance to derive the upstream magnetic field.

2.1. EUV Observations

Since 2010 February, the AIA has been taking full-disk coronal images of the Sun in seven EUV channels representing a wide range of temperatures. The pixel resolution is 0''.6 and the basic cadence is 12 s (see Lemen et al. 2011 for more details of the instrument). Here we sample the images in 193 Å every minute starting from the time the first signatures of the eruption were observed. The eruption occurred from active region NOAA 1079 from the southwest limb (S25W84) in association with an M1.0 flare. Figure 1 shows running difference images, in which we see the evolution of the CME as a series of snapshots from the very early stage at 05:34:54 UT–05:41:54 UT. The shock structure becomes clear in the 05:37:54 UT image and is visible throughout the observation.

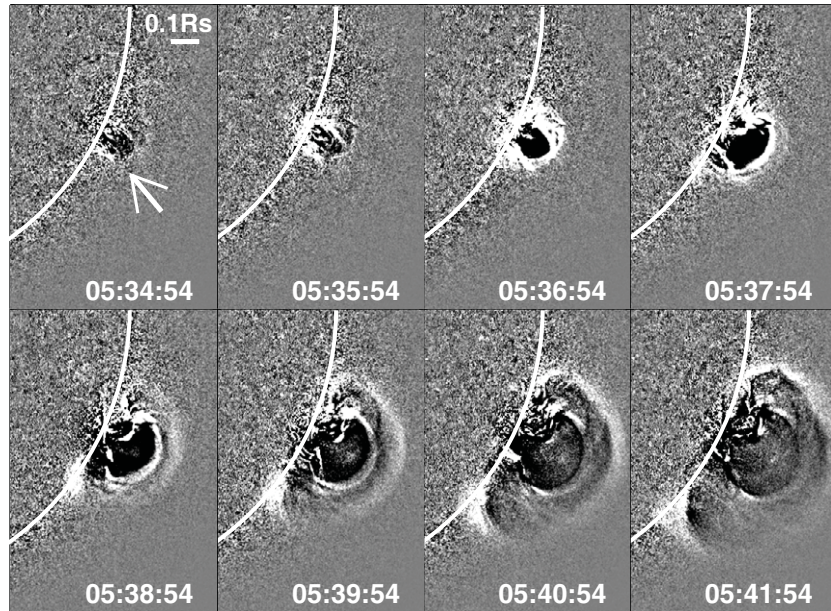


Figure 1. Snapshots of the CME from *SDO/AIA* 193 Å difference images. A small section of the images from the southwest corner is shown. The arrow points to the early stage of the CME. The scale of the images is also indicated on the first frame in terms of a solar radius (R_s). The optical limb is also drawn. A full cadence (12 s) movie of the event is included as an electronic supplement in the online journal.

(An animation and a color version of this figure are available in the online journal.)

The shock structure connects to the EUV wave feature moving away from the eruption site, more clearly seen at later times. This is consistent with the interpretation that the EUV wave is a fast-mode shock surrounding the CME flux rope (see, e.g., Veronig et al. 2010). We identify the inner circular feature as the flux rope that drives the shock. There is a sudden change in the shape of the flux rope indicating rapid expansion in the lateral direction between 05:36:54 and 05:37:54 UT. Interestingly this is the time the shock became distinctly visible. Full-cadence data show that a diffuse structure formed ahead of the flux rope at 05:36:54 UT. This coincided with the onset of the metric type II radio burst (see below). The overall position angle extent (including the shock) was $\sim 37^\circ$ by the time the CME left the *SDO/AIA* field of view (FOV). The flux rope itself subtended an angle of only $\sim 17^\circ$. The CME first appeared in the LASCO/C2 FOV at 06:06 UT, when the leading edge was already at 2.57 R_s . The speed within the LASCO FOV is only 320 km s^{-1} and the CME has a position angle extent of $\sim 33^\circ$. Clearly, the flux rope seems to have decelerated significantly by the time it reached the outer corona. The position angle extent suggests that the LASCO CME must be the expanded flux rope. The CME does not show the diffuse shock structure in the LASCO FOV, suggesting that the shock might have weakened and dissipated by the time it reached the LASCO FOV. Therefore, the speed must have peaked somewhere between 1.5 and 2.57 R_s . Without the *SDO* observations, the connection between the type II burst, the shock, and the flux rope would not have been revealed.

The shock structure is better described in Figure 2 with the projection of the flux rope on the sky plane fitted to a circle. We identify the radius of this circle as the minor radius of the flux rope and also the radius of curvature of the shock driver. The shock itself is not resolved, but the broad diffuse feature ahead of the flux rope is the shock sheath. The leading edge of the shock sheath is expected to be the shock. We identify the position of the leading edge of the sheath as the shock location.

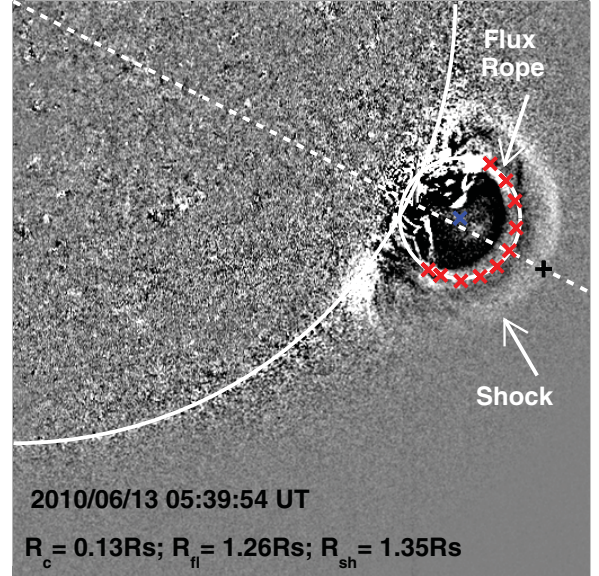


Figure 2. *SDO/AIA* difference image at 193 Å showing the flux rope and the shock structure surrounding it. The heliocentric distances of the shock (R_{sh} , marked by the “+” symbol) and the flux rope (R_f) are shown. The red crosses are the points on the flux rope used for fitting the circle. The blue cross marks the center of the fitted circle. The radius of the circle fitted to the flux rope is the radius of curvature (R_c) of the flux rope.

(A color version of this figure is available in the online journal.)

Thus, the thickness of the sheath becomes the standoff distance of the shock ahead of the flux rope.

The heliocentric distance of the shock (R_{sh}) was measured at six instances from 05:36:54 UT to 05:42:54 UT, traveling from $\sim 1.19 R_s$ to $1.46 R_s$. The flux rope leading edge (R_f) was observed from $\sim 1.13 R_s$ to $1.38 R_s$ before its leading edge left the *SDO/AIA* FOV after 05:43:54 UT. The standoff distance (the difference between R_{sh} and R_f) steadily increased

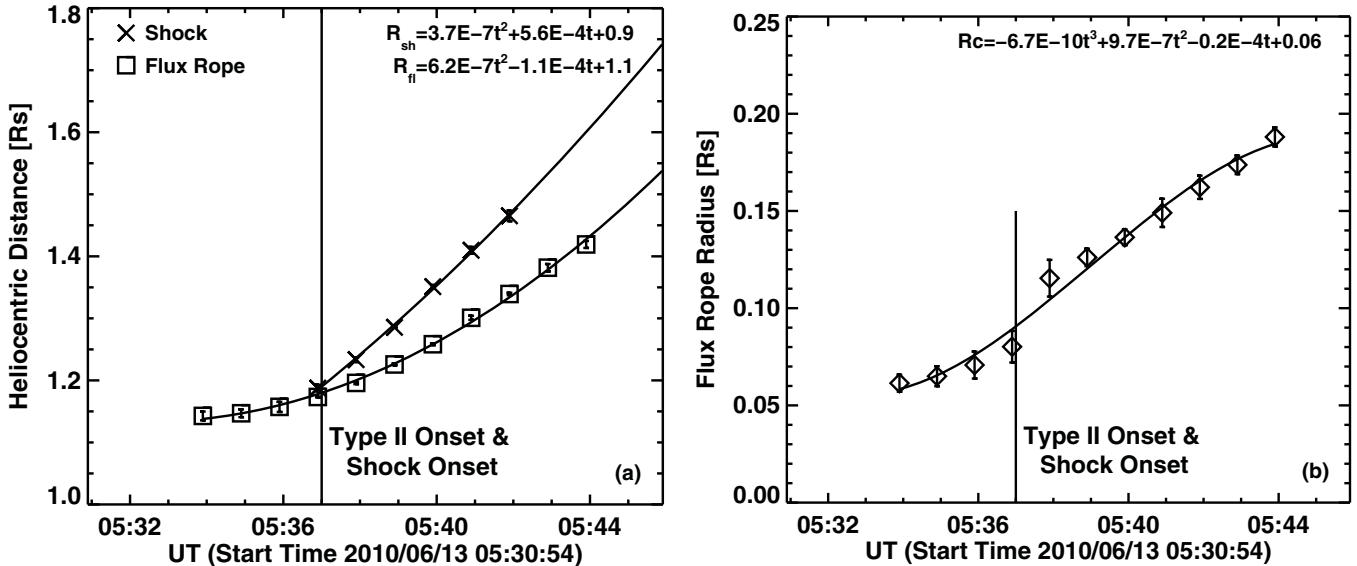


Figure 3. (a) Height–time plot of the shock and flux rope with the quadratic fit to the measurements. All heights refer to the Sun center. One-minute difference images were used. The shock first appeared only at 05:36:54 UT, which coincided with the onset of the metric type II burst. The error bars on the heights give standard deviations of four independent measurements. The equations of the fitted curves are $R_{sh}(t) = 3.7 \times 10^{-7}t^2 + 5.6 \times 10^{-4}t + 0.9$ and $R_{fl}(t) = 6.2 \times 10^{-7}t^2 - 1.1 \times 10^{-4}t + 1.1$, where t is the time in seconds from 05:30:54 UT. (b) Time evolution of the flux rope radius (also known as minor radius) obtained by fitting a circle to the flux rope cross section. The error bars represent the errors in fitting the circle (the maximum error is ± 0.01 Rs with most points having a much lower error). The solid curve is the third-order polynomial fit to the data points, whose equation is $R_c(t) = -6.7 \times 10^{-10}t^3 + 9.7 \times 10^{-7}t^2 - 0.2 \times 10^{-4}t + 0.06$ with t in seconds from 05:30:54 UT.

from ~ 0.02 Rs to 0.13 Rs when both the flux rope and the shock were observed. The flux rope radius is the same as the radius of curvature (R_c), which doubled during the flux rope transit through the *SDO/AIA* FOV. This is a limb event, so we are looking at the cross section of the flux rope, with its axis roughly perpendicular to the sky plane. Note that the radius of curvature of the flux rope is initially similar to half of the flux rope height above the limb, but rapidly increases at the time of shock formation. The eruption is from W84, so the projection effects are expected to be minimal: the true heights and speeds are expected to be larger only by $< 0.6\%$, which is negligible.

Figure 3 shows the height–time plots of the shock, the flux rope, and the radius of the flux rope. The average speeds of the flux rope and shock are 330 km s^{-1} and 644 km s^{-1} , respectively. The average expansion speed of the flux rope is $\sim 160 \text{ km s}^{-1}$. The diameter of the flux rope increases with the same speed as the radial speed of the flux rope. In Figure 3(a), the height–time measurements are fitted with second-order polynomials. Both the flux rope and the shock show increase in speed through the *SDO* FOV. The sudden increase in the flux rope radius between 05:36:54 UT and 05:37:54 UT is associated with the rapid expansion of the flux rope and coincides with the shock formation. A third-order polynomial fit to the flux rope radius shows a complex evolution compared to the leading edge of the flux rope and the shock. From the first three points, we estimate an average expansion speed of $\sim 42 \text{ km s}^{-1}$, which jumps to 136 km s^{-1} by 05:37:54 UT around the time of shock formation. The radial speed of the CME flux rope is only $\sim 245 \text{ km s}^{-1}$ at the time of shock formation.

2.2. Radio Observations

The shock formation observed in EUV remarkably coincided with the onset of a metric type II burst at 05:37:00 UT at the frequency of 300 MHz (harmonic) and 150 MHz (fundamental). Type II radio bursts are emitted at the local plasma frequency

in the vicinity of the shock, so a 150 MHz frequency implies a local plasma density of $2.8 \times 10^8 \text{ cm}^{-3}$, which is consistent with the shock formation close to the solar surface (0.19 Rs above the surface). The radio dynamic spectrum from the Hiraiso Radio Observatory in Figure 4 shows that the fundamental and harmonic components are visible, so there is no ambiguity in relating the emission frequency to the plasma frequency. The harmonic component is visible better than the fundamental component. The average drift rate of the type II burst is $\sim 0.28 \text{ MHz s}^{-1}$, which is typical of metric type II bursts (see Gopalswamy et al. 2009). The harmonic component also shows band splitting, which indicates that the emission comes from behind and ahead of the shock (Smerd et al. 1974; Vrsnak et al. 2004; Cho et al. 2007). At the five times marked in Figure 4, the upper (f_2) and lower (f_1) bands are at frequencies (186, 156), (162, 128), (146, 118), (128, 104), (115, 90) MHz, indicating an average separation of $\sim 28 \text{ MHz}$. The frequency ratio f_2/f_1 is directly related to the density jump across the shock because f_1 and f_2 correspond to emission ahead and behind the shock. The average value of $f_2/f_1 = 1.24$, which corresponds to a density compression of 1.54 across the shock.

To derive the magnetic field from the Alfvén speed, one needs the ambient plasma density at the shock nose. For the 2010 June 13 event, we can use the type II radio burst observations to get the plasma density because the emission takes place at the local plasma frequency (f_p) and its second harmonic ($2f_p$). Since $f_p = 9 \times 10^{-3}n^{1/2} \text{ MHz}$ with the electron density n in cm^{-3} , one can obtain n from the dynamic spectrum by identifying f_p . The emission ahead of the shock is from the unshocked corona, so the emission occurs at a lower frequency (f_1) compared to the compressed downstream ($f_2 > f_1$). We need to use the lower frequency (f_1) to get the upstream plasma frequency (f_{p1}) and density (n_2): $f_{p1} = f_1/2$. Figure 4 shows that the band splitting is clear between 05:39:30 and 05:43:30 UT. Three of the *SDO/AIA* frames overlap with this interval: at 05:39:54, 05:40:54, and 05:41:54 UT, so we get $f_1 = 128, 118$, and

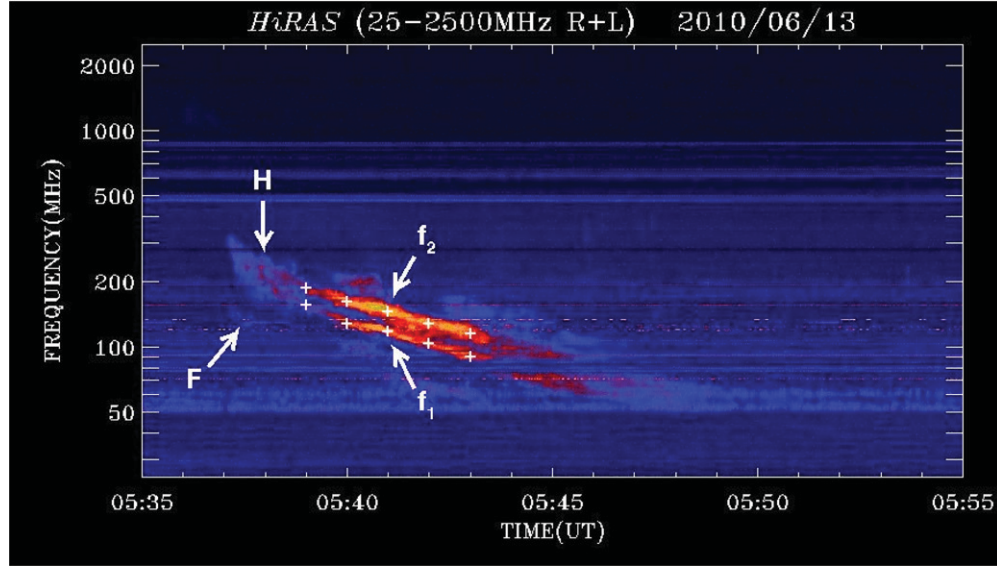


Figure 4. Radio dynamic spectrum from the Hiraiso Radio Spectrograph (HiRAS) showing the type II burst starting from \sim 05:37 UT until about 05:47 UT beyond which it is masked by the interference in the 50–60 MHz frequency range. The band splitting is clear between 05:39:30 and 05:43:30 UT.
(A color version of this figure is available in the online journal.)

104 MHz giving the upstream densities (n_2) as 5.1, 4.3, and 3.3 in units of 10^7 cm^{-3} at these times.

2.3. Coronal Magnetic Field

The standoff distance method to derive the coronal magnetic field involves measuring the leading edges of the CME flux rope (R_{fl}) and the leading shock (R_{sh}) at the nose and measuring the radius of curvature (R_c) of the flux rope fitted to a circle (see Gopalswamy & Yashiro 2011). The standoff distance $\Delta R = R_{\text{sh}} - R_{\text{fl}}$ is related to the shock Mach number (M) and the adiabatic exponent (γ ; Russell & Mulligan 2002):

$$\Delta R / R_c = 0.81[(\gamma - 1)M^2 + 2]/[(\gamma + 1)(M^2 - 1)]. \quad (1)$$

Here we take the Mach number to be the Alfvén Mach number. In terms of the relative standoff distance $\delta = \Delta R / R_c$, the Mach number can be written as

$$M^2 = 1 + [1.24\delta - (\gamma - 1)/(\gamma + 1)]^{-1}. \quad (2)$$

Measuring δ and assuming γ , one can get the Alfvén Mach number. Note that the second term on the right-hand side of Equation (2) needs to be positive for a shock, which imposes a minimum value of $\delta = 0.115$ for $\gamma = 4/3$ and 0.202 for $\gamma = 5/3$. In order to get the magnetic field strength (B), we need the upstream Alfvén speed (V_A) and the plasma density (n). Since $V_A = V_{\text{sh}}/M$, where the shock speed V_{sh} is obtained from the time series of R_{sh} measured in the EUV images. In the coronal region we are interested in, the solar wind speed is negligible compared to the shock speed. The magnetic field strength in the upstream medium is given by

$$B = 4.59 \times 10^{-7} V_A n^{1/2} \text{ G}. \quad (3)$$

All we need is the upstream density, which can be derived directly from the emission frequency of the type II burst as explained in Section 2.2. For example, at 05:40 UT, the upper and lower bands of the harmonic component have frequencies $f_2 = 162$ and $f_1 = 128$ MHz, respectively. The local plasma frequencies are therefore $f_{p2} = 81$ and $f_{p1} = 64$ MHz, respectively,

corresponds with $n_1 = 5.1 \times 10^7 \text{ cm}^{-3}$. At 05:39:54 UT, we measure $\Delta R = 9.1 \times 10^{-2} \text{ Rs}$ and $R_c = 0.134 \text{ Rs}$, so $\delta = 0.68$, which when substituted in Equation (2) with $\gamma = 4/3$ gives $M = 1.56$. We use R_{sh} measured at 05:38:54 UT and 05:40:54 UT, to get the local shock speed at 05:39:54 UT as $V_{\text{sh}} \sim 721 \text{ km s}^{-1}$, which in turn gives $V_A = V_{\text{sh}}/M = 462 \text{ km s}^{-1}$. Putting $n = 5.1 \times 10^7 \text{ cm}^{-3}$ and $V_A = 462 \text{ km s}^{-1}$ in Equation (3), we get $B = 1.51 \text{ G}$ corresponding to a heliocentric distance of 1.35 Rs. Dulk & McLean (1978) derived the radial dependence

$$B(r) = 0.5(r - 1)^{-1.5}, \quad (4)$$

where r is the heliocentric distance. At $r = 1.35 \text{ Rs}$, this formula gives $B = 2.4 \text{ G}$, which is $\sim 60\%$ higher than our value.

Table 1 shows the derived magnetic field values for the times during which the shock and radio measurements are available. The magnetic field also declines steadily within the *SDO/AIA* FOV. Note that the flux rope was observed before the shock formation and the shock left the *SDO/AIA* FOV before the flux rope did. The Mach number was determined assuming $\gamma = 4/3$. The numbers in parentheses correspond to $\gamma = 5/3$. The Mach number steadily declines from 3.72 in the beginning to 1.49 just before the shock left the *SDO* FOV. The ambient Alfvén speed steadily increases, reaching a maximum of 462 km s^{-1} and then declines by a few percent in the next two measurements. The Alfvén speed decline directly reflects the decrease in the local shock speed obtained from three consecutive height-time measurements of the shock (except for the first and last measurements). It is possible that the shock indeed begins to weaken around this time, but we do not have sufficient information because of the limited *SDO* FOV.

The numbers in Table 1 are shown graphically in Figure 5. The Alfvén speed of the corona in Figure 5(a) is obtained using the “local shock speed” method described above. In Figure 5(b), the shock speeds used are from the quadratic fit shown in Figure 3(a). The slight decline in Alfvén speed is likely to be a local fluctuation, which is smoothed out by the quadratic fit. The Mach number declines through the *SDO/AIA* FOV in both cases because its derivation does not depend on the shock speed. The lower γ value results in a higher Alfvén Mach number. The

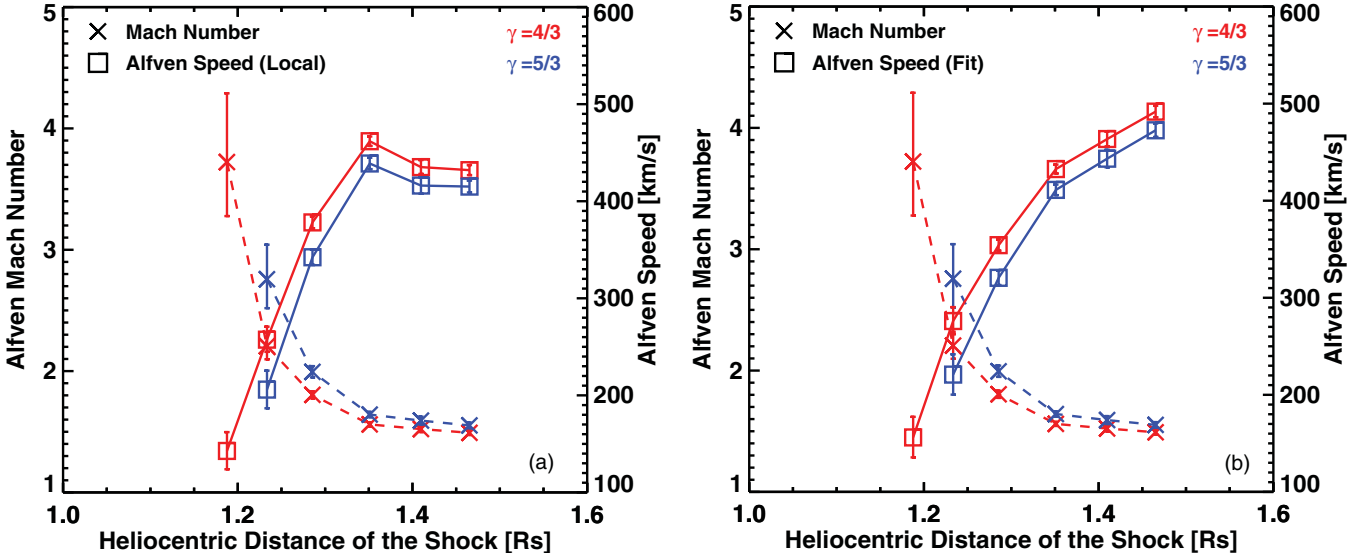


Figure 5. (a) Derived Mach number and Alfvén speed for $\gamma = 4/3$ and $5/3$. The Alfvén speed was derived using local shock speed obtained from three consecutive height–time measurements. (b) Same as in panel (a) except that the Alfvén speed is obtained using a shock speed derived from a second-order fit to the height–time plot (see Figure 3(a)).

(A color version of this figure is available in the online journal.)

Table 1.
Shock and Flux Rope Measurements and the Derived Properties of the Corona for $\gamma = 4/3$ ($5/3$)

Time UT	R_{sh} (Rs)	R_{fl} (Rs)	ΔR (Rs)	R_c (Rs)	δ	V_{sh} (km s $^{-1}$)	f_{p1} (MHz)	n_1 ($\times 10^7$) cm $^{-3}$	M	V_A (km s $^{-1}$)	B (G)
05:34:54	...	1.15
05:35:54	...	1.16
05:36:54	1.19	1.17	0.014	0.080	0.18	531	3.72 (...)	143 (...)	...
05:37:54	1.23	1.20	0.037	0.115	0.32	568	2.21 (2.76)	257 (206)	...
05:38:54	1.29	1.23	0.060	0.126	0.47	682	78	7.5	1.80 (1.99)	378 (342)	1.50 (1.36)
05:39:54	1.35	1.26	0.092	0.136	0.68	721	64	5.1	1.56 (1.64)	462 (439)	1.51 (1.43)
05:40:54	1.41	1.30	0.108	0.149	0.73	663	59	4.3	1.52 (1.59)	435 (416)	1.31 (1.25)
05:41:54	1.47	1.34	0.126	0.162	0.77	644	52	3.3	1.49 (1.55)	432 (415)	1.15 (1.10)
05:42:54	1.38	45	2.5

Alfvén speed on the other hand is lower for the higher value of γ because for a given shock speed, the Alfvén speed is inversely proportional to the Mach number. Weakening of the shock is evident even when the shock speed is increasing because of the rapid increase in the ambient Alfvén speed. It appears that the present observations correspond to the increasing leg of the Alfvén speed close to the coronal base (Mann et al. 1999, 2003; Gopalsamy et al. 2001). Gopalsamy et al. (2001) found that the Alfvén speed starts increasing around a heliocentric distance of 1.4 Rs. In the present case, the increase seems to have started a bit closer to the Sun. As noted before, the shock seems to have dissipated by the time the CME reached the LASCO/C2 FOV.

Figure 6 shows the derived magnetic fields from the shock measurements for $\gamma = 4/3$ and $5/3$ at four instances when the upstream plasma density is available from the radio observations. Our magnetic field value at the lowest height is not reliable because the band splitting is not clear (see Figure 4). Also shown are the Dulk & McLean (1978) empirical relations for the magnetic field in the active region corona and a quiet-Sun magnetic field model $B(r) = a/r^2$ with two values of the constant a : 2.2 and 2.6. Our values are closest to the quiet-Sun curve with $a = 2.6$. The model curves show that the active region blends with the quiet corona around 1.4 Rs (see also Gopalsamy et al. 2001); in the present case, it seems to have happened at a lower heliocentric distance.

The active region was very small and had an area of only 10 msh (http://kukui.ifa.hawaii.edu/ARMaps/Archive/2010/20100613.1632_armpng). Therefore, it is likely that the quiet corona became dominant at lower altitudes than expected. Magnetic field values from other techniques are shown for comparison: Fineschi et al. (1999), Mancuso et al. (2003), and Cho et al. (2007). These values are in general agreement with ours, except for the Fineschi et al. (1999) data point at 1.4 Rs.

2.4. Shock Compression Ratio

Finally, we check the consistency of our analysis from the compression ratio (downstream density n_2 to upstream density n_1) obtained from band splitting to the theoretical value. From the dynamic spectrum, n_2/n_1 is simply $(f_{\text{p2}}/f_{\text{p1}})^2 = (f_2/f_1)^2$. For the four instances in Figure 4 we get the compression ratio as 1.42, 1.60, 1.53, and 1.51. The first of these values is not very accurate because the split bands are not very well defined at this time. Assuming that the shock is quasi-perpendicular at these low heights, we can use the simplified formula (Draine & McKee 1993),

$$n_2/n_1 = 2(\gamma + 1)/\{D + [D^2 + 4(\gamma + 1)(2 - \gamma)M^{-2}]^{1/2}\}, \quad (5)$$

where $D = (\gamma - 1) + (2/M_s^2 + \gamma/M^2)$ and $M_s = V_{\text{sh}}/C_s$ is the sonic Mach number. For a 2 MK corona, the sound speed

Table 2.
Shock Properties from Theory and Measurements for $\gamma = 4/3$ (5/3) and Sound Speed = 128 km s $^{-1}$

Time (UT)	R_{sh} (Rs)	V_{sh} (km s $^{-1}$)	M	M_s	n_2/n_1 (Radio)	n_2/n_1 (Theory)	β
05:38:54	1.29	682	1.80 (1.99)	5.33	1.42	1.93 (2.01)	0.11 (0.14)
05:39:54	1.35	721	1.56 (1.64)	5.63	1.60	1.67 (1.71)	0.08 (0.09)
05:40:54	1.41	663	1.52 (1.59)	5.18	1.53	1.61 (1.65)	0.09 (0.09)
05:41:54	1.47	644	1.49 (1.55)	5.03	1.51	1.57 (1.61)	0.09 (0.10)

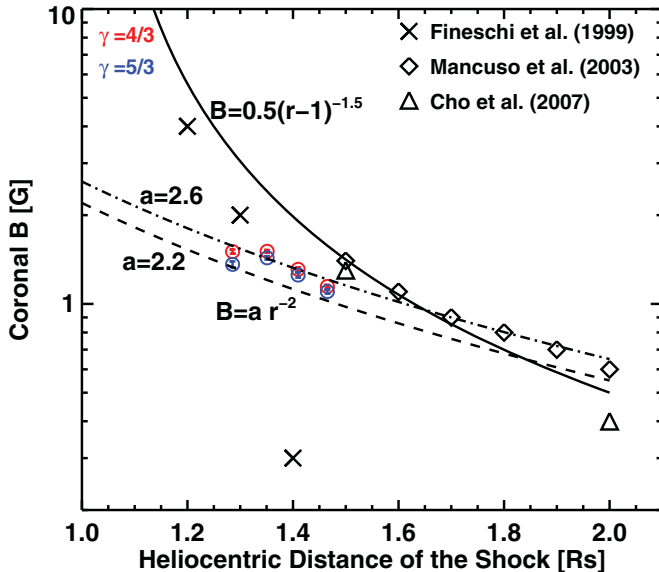


Figure 6. Derived coronal magnetic field values for $\gamma = 4/3$ and $5/3$ using the plasma densities inferred from the lower sideband of the type II radio burst. The Dulk & McLean (1978) empirical relation for the magnetic field above active region $[B(r) = 0.5(r - 1)^{-1.5}]$ corona and a quiet-Sun magnetic field model $B(r) = a/r^2$ with $a = 2.2$ and 2.6 are also shown. Magnetic field values from other techniques are shown for comparison.

(A color version of this figure is available in the online journal.)

$C_s \sim 128$ km s $^{-1}$, so $M_s \sim 5$ for the measured shock speeds. Ma et al. (2011) estimated an upstream temperature of 1.8 MK, similar to the value assumed here. Substituting for M and M_s and taking $\gamma = 4/3$ in Equation (5), we get n_2/n_1 consistent with the values derived from the radio dynamic spectrum (see Table 2). The first value of n_2/n_1 shows the largest deviation, but the radio measurements are not very accurate for this time. The compression ratio and magnetic field strength obtained by Ma et al. (2011) at one instance (05:40 UT) are consistent with our values. Note that Ma et al. (2011) did not use the standoff distance technique to get the magnetic field. Table 2 also shows the plasma beta ($\beta = C_s^2/V_A^2$) using $C_s = 128$ km s $^{-1}$ and V_A from Table 1. The values are consistent with a low beta corona as expected.

3. DISCUSSION

The primary finding of this paper is that the shock structure surrounding the CME flux rope near the Sun can be used to infer the coronal magnetic field strength. The shock standoff distance and the radius of curvature of the flux rope are directly related to the Alfvénic Mach number of the shock and the adiabatic index. From the measured shock speed, we obtained the Alfvén speed assuming the adiabatic exponent. From the emission frequency of the type II radio burst produced by the shock, we get the upstream plasma density and combine

it with the Alfvén speed to get the coronal magnetic field strength. The magnetic field strength obtained is consistent with other estimates from different techniques. Given the paucity of coronal magnetic field measurements, this technique will prove to be very useful in obtaining the field strengths in the coronal region where energetic events originate. Acceleration of energetic particles by CME-driven shocks occurs around or above the heliocentric distances considered here, and hence our results provide useful constraints on the magnetic field strength involved in shock acceleration theories. The magnetic field measurement is also important in providing ground truth to the extrapolation techniques commonly employed in obtaining coronal magnetic fields from the photospheric or chromospheric magnetograms. CME measurements have become routine and the shock structure is readily discerned from white light and EUV observations, so this technique can be used whenever a CME drives a shock. Normally CME observations are used in deriving the properties of eruptive events, but here we have used them to derive the properties of the ambient medium through which the CME-driven shock propagates.

In the analysis we have tacitly assumed that the radio emission comes from near the nose of the shock. We have no imaging observation at radio wavelengths, so we cannot justify this assumption. However, at such low heights in the corona, we do expect the shock to be quasiperpendicular at most locations, so the nose region certainly is favored because of the highest shock strength. If the radio emission originates from the flanks of the shock, then the estimated magnetic field corresponds to a slightly lower height. Note that the overall position angle extent is only $\sim 33^\circ$, so when the nose is at 1.4 Rs, the flank 15° away from the nose is at a height of only 1.35 Rs. By assuming that the radio source is located at the nose, we are making an error of $\sim 4\%$ in the height at which the field estimate is made. It is also possible that the radio emission comes from an extended region around the nose where the Mach number is significantly greater than 1, so the height of the shock nose is a representative height. It must be pointed out that the upstream density can be obtained by other means such as spectroscopic observations and coronal brightness measurements (see, e.g., Bemporad & Mancuso 2010). In this respect, our method of obtaining the Alfvén speed is robust and can utilize density measurements from many different instruments/techniques to obtain the magnetic field.

The derived Alfvén speed in the low corona is consistent with previous estimates based on models of density and magnetic field in the corona (Mann et al. 1999, 2003; Gopalswamy et al. 2001; Warmuth & Mann 2005). In particular, Gopalswamy et al. (2001) estimated that the minimum in the fast-mode speed occurs around 1.4 Rs and could be as low as 230 km s $^{-1}$ and the speed increases at larger heights. The Alfvén speed shown in Figure 5 is consistent with this estimate. The magnetic scale height is much larger than the heliocentric distance range over which we made the magnetic field measurements. For example,

an inverse-square dependence of the magnetic field strength gives a scale height of ~ 2.8 Rs at 1.4 Rs. Our magnetic field measurement corresponds to a distance range of only 0.3 Rs around 1.4 Rs. Thus, it is difficult to obtain the radial profile of the magnetic field. Nevertheless, we see a slight declining trend in the field strength within this range. Gopalswamy & Yashiro (2011) obtained the radial profile of the magnetic field in the outer corona from the standoff distance technique and found that the profile is flatter than the inverse-square dependence. We are in the process of investigating the reasons, one of which could be the usage of the minor radius of the flux rope, while the major radius could be deciding the standoff distance. This difference does not seem to matter very close to the Sun, where the whole eruption appears spherical. The radial and azimuthal components of the magnetic field need to be carefully separated because only the radial component has the inverse-square radial dependence.

4. CONCLUSIONS

Based on the geometrical relationship between the CME flux rope and the shock driven by it discerned from EUV images obtained by *SDO/AIA*, we were able to determine the Alfvénic Mach number in the corona at heliocentric distance range 1.2–1.5 Rs. The Mach number is in the range of 3.7–1.5 (assuming $\gamma = 4/3$) indicating shock weakening within the FOV of the imager. From the measured shock speed and the derived Mach number, we found the Alfvén speed to increase from ~ 140 km s $^{-1}$ to 460 km s $^{-1}$ over the distance range in question. By deriving the upstream plasma density from the emission frequency of type II radio burst, we were able to derive the coronal magnetic field to be in the range of 1.5–1.3 G over a restricted distance range (1.3–1.5 Rs). The derived magnetic field values are consistent with other estimates in a similar distance range, thus the EUV imagers and coronagraphs can be used as coronal magnetometers. The shock compression ratio determined from the band splitting of type II radio burst is also consistent with that derived from shock theory.

Work supported by NASA's LWS program.

REFERENCES

- Bemporad, A., & Mancuso, S. 2010, *ApJ*, **720**, 130
 Bennett, L., Kivelson, M. G., Khurana, K. K., Frank, L. A., & Paterson, W. R. 1997, *J. Geophys. Res.*, **102**, 26927
 Cho, K.-S., Lee, J., Gary, D. E., Moon, Y.-J., & Park, Y. D. 2007, *ApJ*, **665**, 799
 Draine, B. T., & McKee, C. F. 1993, *ARA&A*, **31**, 373
 Dulk, G. A., & McLean, D. J. 1978, *Sol. Phys.*, **57**, 279
 Farris, M. H., & Russell, C. T. 1994, *J. Geophys. Res.*, **99**, 17681
 Fineschi, S., van Ballegoijen, A., & Kohl, J. L. 1999, in 8th SOHO Workshop, Plasma Dynamics and Diagnostics in the Solar Transition Region and Corona, ed. J.-C. Vial & B. Kaldeich-Schümann (ESA SP 446; Noordwijk: ESA), 317
 Gold, T. 1955, in Gas Dynamics of Cosmic Clouds, Discussion of Shock Waves and Rarefied Gases, ed. J. C. van de Hulst & J. M. Burgers (Amsterdam: North-Holland), 193
 Gold, T. 1962, *Space Sci. Rev.*, **1**, 100
 Gopalswamy, N., Lara, A., Kaiser, M. L., & Bougeret, J.-L. 2001, *J. Geophys. Res.*, **106**, 25261
 Gopalswamy, N., Thompson, W. T., Davila, J. M., et al. 2009, *Sol. Phys.*, **259**, 227
 Gopalswamy, N., & Yashiro, S. 2011, *ApJ*, **736**, L17
 Kondo, T., Isobe, T., Igi, S., Watari, S.-I., & Tokumaru, M. 1997, *Rev. Commun. Res. Lab.*, **43**, 231
 Kozarev, K. A., Korreck, K. E., Lobzin, V. V., Weber, M. A., & Schwadron, N. A. 2011, *ApJ*, **733**, L25
 Lemen, J. R., Title, A. M., Akin, D. J., et al. 2011, *Sol. Phys.*
 Ma, S.-L., Raymond, J. C., Golub, L., et al. 2011, *ApJ*, **738**, 160
 Mancuso, S., Raymond, J. C., Kohl, J., et al. 2003, *A&A*, **400**, 347
 Mann, G., Klassen, A., Aurass, H., & Classen, H.-T. 2003, *A&A*, **400**, 329
 Mann, G., Klassen, A., Estel, C., & Thompson, B.J. 1999, in Proc. of 8th SOHO Workshop, Plasma Dynamics and Diagnostics in the Solar Transition Region and Corona, ed. J.-C. Vial & B. Kaldeich-Schümann (ESA SP 446; Noordwijk: ESA), 477
 Ontiveros, V., & Vourlidas, A. 2009, *ApJ*, **693**, 267
 Patsourakos, S., Vourlidas, A., & Stenborg, G. 2010, *ApJ*, **724**, L188
 Russell, C. T., & Mulligan, T. 2002, *Planet. Space Sci.*, **50**, 527
 Schwer, K., Lilly, R. B., Thompson, B. J., & Brewer, D. A. 2002, AGU Fall Meeting, Abstract SH21C-01
 Smerd, S. F., Sheridan, K. V., & Stewart, R. T. 1974, in IAU Symp. 57, Coronal Disturbances, ed. G. A. Newkirk (Boston: Reidel), 389
 Sonett, C. P., Colburn, D. S., Davis, L., Smith, E. J., & Coleman, P. J. 1964, *Phys. Rev. Lett.*, **13**, 153
 Veronig, A. M., Muhr, N., Kienreich, I. W., Temmer, M., & Vršnak, B. 2010, *ApJ*, **716**, L57
 Vršnak, B., Magdalenić, J., & Zlobec, P. 2004, *A&A*, **413**, 753
 Warmuth, A., & Mann, G. 2005, *A&A*, **435**, 1123